Heliyon 8 (2022) e12531

Contents lists available at ScienceDirect

Heliyon

journal homepage: www.cell.com/heliyon

Research article

Study on the effect of the size irregularity gradient of metal foams on macroscopic compressive properties

Xiaoyang Zhang [a], Liqun Tang [b,*], Bao Yang [b], Heping Hu [a], Shifeng Tan [a]

[a] School of Mathematics and Physics, University of South China, 421001, Hengyang, Hunan, China
[b] Department of Engineering Mechanics, School of Civil Engineering and Transportation; State Key Laboratory of Subtropical Building Science, South China University of Technology, 510641, Guangzhou, Guangdong, China

HIGHLIGHTS

- Density gradient is not enough to describe mechanical properties of gradient foams.
- A theoretical model is developed to describe stress–strain curves.
- The nominal stress is a linear function of the current relative density.

ARTICLE INFO

Keywords:
Size irregularity gradient
Gradient metal foam
Theoretical model
Deformation mechanism
Compressive properties

ABSTRACT

Size irregularity gradient and cell wall gradient, combined as the density gradient in previous studies, affect the macroscopic mechanical properties of the gradient metal foam. More and more complex mesostructures are designed and applied in metal foams, and the density gradient becomes insufficient to describe the difference in mesostructures. To explore the effect of mesostructures carefully, this study focuses on the effect of the size irregularity gradient on the macroscopic compressive properties of metal foams. A series of metal foam models were developed using the 3D Voronoi technique. These models have the same average relative densities, the same average diameters and different size irregularity gradients. Simulation results indicated that the macroscopic mechanical properties of cell wall gradient metal foams are significantly different from those of size irregularity gradient metal foams, though these models have the same relative density gradient. To explore the effect of size irregularity gradient, a theoretical model was developed to characterize the compression process from the first cell-collapse to full condensation. Theoretical results showed a linear relationship between the nominal stress and the current relative density. These findings can provide efficient guidance for the design and applications of gradient metal foams.

1. Introduction

Foams, particularly gradient metal foams, are important functional materials that offer advantages such as low weight and high specific strength and energy absorption efficiency [1, 2, 3, 4, 5, 6, 7, 8, 9, 10]. They are widely used in applications requiring superior energy absorption and structural protection [11, 12, 13, 14, 15, 16, 17, 18, 19, 20]. Their unique energy absorption properties are strongly dependent on the cell structure; therefore, several studies have focused on this aspect. The relationship between the density gradient and macroscopic mechanical properties of metal foam has been studied via experimental and theoretical approaches [12, 13, 15, 21, 22, 23, 24]. In these studies, the size irregularity gradient and cell wall gradient have been modeled as the density gradient. Consequently, their influence on the macroscopic mechanical properties of metal foams has not been adequately distinguished. However, the mesostructural morphology, which is generally characterized by mesostructural irregularity [25, 26, 27, 28, 29], has been found to affect the mechanical properties and deformation of foams [11, 25, 26, 29, 30, 31, 32]. Therefore, it is important to examine the effects of the size irregularity gradient of metal foams on their macroscopic mechanical properties.

With the development of manufacturing techniques [8, 12, 13, 16, 33, 34, 35, 36], several kinds of gradient foams have been produced [11, 12, 13, 16, 22, 33, 37]. Several experiments [12, 16, 22, 33, 37] and

* Corresponding author.
E-mail address: lqtang@scut.edu.cn (L. Tang).

https://doi.org/10.1016/j.heliyon.2022.e12531
Received 15 September 2022; Received in revised form 22 November 2022; Accepted 14 December 2022

simulations [11, 15, 18, 22, 38] have been performed to investigate the quasi-static [12, 16] and dynamic responses [18, 31, 37, 38, 39] of gradient foams. The stress–strain curves of metal foams generally have an elastic region, a plastic region with cell collapse and a dense region. During the plastic region, uniform foams show a flat plateau [29, 40, 41, 42], while gradient foams exhibit an obvious strain-hardening phenomenon in the plastic region [11, 16, 33]. Moreover, the gradient structures have been compressed in a layer-by-layer sequence [11, 12, 16, 33]. Duan et al. [11] experimentally observed that the deformation region of size irregularity gradient foam was significantly smaller than that of cell wall gradient foam with identical relative density gradient. Both discrete [22, 24, 31] and continuous [16, 43] size irregularity gradient foams have been constructed using the Voronoi technique to examine macroscopic properties such as the effective elastic modulus, reaction force, densification strain, and energy absorption. Based on the assumption that gradient structures can be replaced by uniform structures with the same relative density using a layer-by-layer method [16, 18], a few theoretical models have been proposed to characterize the compressive response of gradient foams based on relative density gradient [16, 43, 44]. Duan et al. [16] constructed an elastic, plastic-hardening, and locking (E-PH-L) model to describe the elastic, strain-hardening, and densification characteristics of gradient foams. They assumed that the stress of the local structure of gradient foams could be replaced by the collapse stress of uniform foam with the same relative density and thickness. This replacement could be inaccurate for size irregularity gradient foams because the local deformation of structures of gradient foam differs from that of uniform foam, and the deformation of the local structures of gradient foams could be too large for the attainment of the densification stage rather than the plateau stage. Therefore, it is essential to establish an accurate constitutive model with the size irregularity gradient based on the deformation mechanism and matrix properties to characterize the macro compressive mechanical properties of size irregularity gradient metal foams (SIGMFs).

Mesostructural irregularity has been defined to characterize the complex mesostructures of foams [25, 26, 27, 28, 29]. Tang et al. [25] defined two irregularities for each cell, namely shape irregularity R_a and size irregularity R_i. These are expressed as follows:

$$R_a = \frac{\sqrt{A/4\pi}}{\sqrt[3]{3V/4\pi}} - 1,\ R_i = \frac{d - d_0}{d_0} \tag{1}$$

where $A, V,$ and d are the surface area, volume and equivalent diameter, respectively, of the cell; and d_0 is the mean equivalent diameter of the foam model. It can be determined using Eq. (2) with the total volume V_0 and number of cells N.

$$d_0 = \sqrt[3]{\frac{6V_0}{\pi N}} \tag{2}$$

The shape irregularity and size irregularity characterize the shape and size features, respectively, of a cell. The statistical parameters of irregularity of all cells can be used to describe the complex mesostructure of foams. The effects of the shape irregularity gradient of metal foams on their compressive properties have been examined in previous studies [22, 24, 31]. Therefore, in this study, we focused on the effect of the size irregularity gradient of metal foams on their macroscopic compressive properties.

In this study, a series of finite element models of metal foam was developed using the 3D Voronoi technique. These models have equal average relative densities and average equivalent diameters. However, these possess different size irregularity gradients. The effects of the size irregularity gradient of the metal foams on the quasi-static compressive responses were examined. In addition, the deformation mechanism was analyzed. And then, a theoretical model was developed to characterize the compression process of the SIGMF from the first cell-collapse to the full condensation. We verified the model using numerical simulation results and previous experimental results. The findings of this study can provide an effective guidance for design and applications of gradient metal foams.

2. Finite element model of SIGMF

2.1. Construction of SIGMF

The size irregularity R_i of a cell varies linearly with its equivalent diameter d according to Eq. (1). Therefore, controlling the specified minimum distance function $d(x, y, z)$ between any two seeds could be effective method to determine the spatial distribution of size irregularity.

To construct models with a size irregularity gradient in a specified direction (such as the x-direction), the minimum distance function $d(x, y, z)$ between any two seeds should be a linear function of the x-coordinate (the modified voro++ [45] program is employed), as follows:

$$d(x, y, z) = a \cdot x / w_0 + b \tag{3}$$

where w_0 is the length of the 3D Voronoi model in the x-direction and $x \in [0, w_0]$ is the seed position of a cell in the gradient direction. Furthermore, $a \geq 0,\ b \geq 0$. The parameter a affects the gradient degree of mesostructures. The gradient distribution of size irregularity of foam models becomes more obvious with increase of either a or b. According to Eq. (3), the maximum, minimum, and mean values can be determined as follows.

$$d(x, y, z)|_{\max} = a + b, d(x, y, z)|_{\min} = b, d(x, y, z)|_{\text{mean}} = a / 2 + b \tag{4}$$

For a cubic 3D Voronoi model with length w_0, mean equivalent diameter d_0, and number of cells N, Eq. (5) should be satisfied.

$$d(x, y, z)|_{\text{mean}} = d_0, V_0 = w_0^3 \tag{5}$$

To eliminate the boundary effect of foams, the number of cells should be at least seven in each direction [1]. Therefore,

$$w_0 \geq 7 \cdot d(x, y, z)|_{\max} \tag{6}$$

The quantitative relationships of a and b with d_0, w_0, N could be derived by combining Eqs. (2), (4), (5), and (6).

Considering that the actual distance between two seeds would be larger than or equal to the corresponding value of the minimum function $d(x, y, z)$, the actual number of cells N_1 of the constructed 3D Voronoi model may be smaller than the preset value N. The rationality of the constructed models can be verified by examining the difference between N_1 and N. If the difference is excessive, the constructed gradient foam is irrational, and the values of modeling parameters should be modified. The number of cells N should be 1500 for the cubic 3D Voronoi model with length $w_0 = 30$ mm, making sure that the mean equivalent diameter of SIGMF equals to that of the aluminum foam specimen: 3.25 mm [40].

A series of 3D Voronoi models with different size irregularity gradients and equal average relative density and average equivalent diameter was constructed (Figure 1) with specific modeling parameters (Table 1). The $Y = 0$ cross-sectional structures are shown in Figure 2. The 3D Voronoi models possess the more gradient of the cells' size with increase of either a or b. When b is excessively small, there is no apparent gradient feature in the low x regions. This may be mainly because the actual seed distance would differ marginally from the value of Eq. (3). To evaluate the repeatability of the SIGMF construction method, three size irregularity gradient 3D Voronoi models were constructed with the same modeling parameters: $a = 3$ mm, $b = 0$ mm, $w_0 = 30$ mm, $N = 1500$. The spatial distributions of the size irregularity of these gradient models nearly coincide with each other as shown in Figure 3. These results indicated that the proposed method for constructing the gradient 3D Voronoi model has good repeatability.

To investigate whether the density gradient is sufficient for describing the macroscopic properties of gradient foams, a cell wall gradient 3D

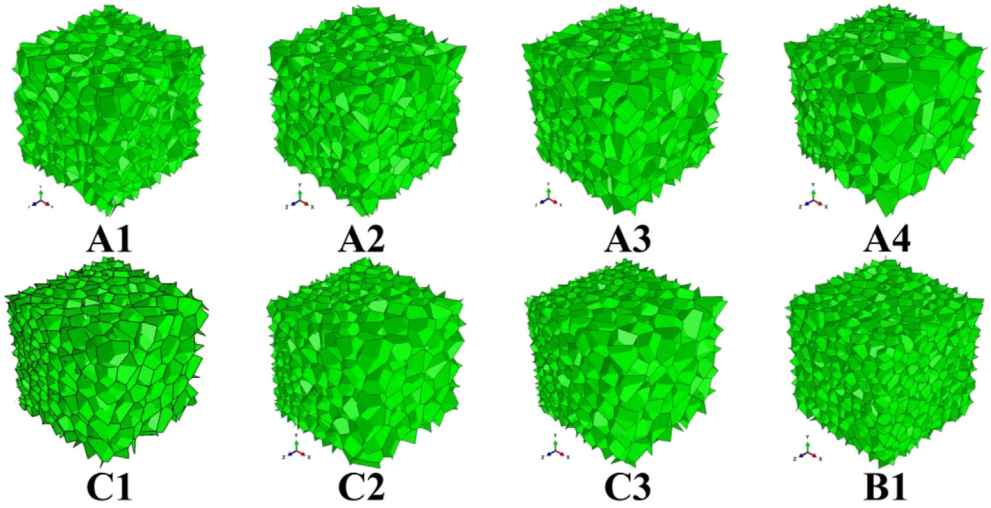

Figure 1. Gradient 3D Voronoi models with different modeling parameters: for A1–A4 foams, the parameter a increases from 0 to 4 mm while the parameter b be constant zero; for C1–C3 foams, the parameter b increases from 0.7 mm to 1.3 mm while the parameter a be constant 3 mm; for B1 foam, parameters a and b equal to 0 and 2.15 mm, respectively.

Table 1. Modeling parameters and gradient parameter of size irregularity gradient 3D Voronoi models.

Model	a (mm)	b (mm)	N	w_0 (mm)	Gradient parameter k
A1	0	0	1500	30	−0.026
A2	2	0	1500	30	0.257
A3	3	0	1500	30	0.633
A4	4	0	1500	30	1.150
B1	0	2.15	1500	30	-0.024
C1	3	0.7	1500	30	1.04
C2	3	1.0	1500	30	1.138
C3	3	1.3	1500	30	1.167

Voronoi model named B1T was constructed based on the B1 model with a specific thickness gradient function. Its probability of shape irregularity is equal to that of the C3 model (shown in Figure 4). In addition, its density gradient is the same as that of the C3 model. Whether the density gradient is sufficient to characterize the macroscopic mechanical properties of the two types of gradient foams can be verified by comparing the compressive responses of the B1T model with those of the C3 model.

2.2. Features of SIGMF

2.2.1. Spatial distribution of size irregularity

The position of each cell can be represented by the seed position. Thereby, the spatial distribution of the size irregularity can be described. For example, the spatial distribution of the size irregularity of the C3 model is shown as black scatters in Figure 5(a). These scatter data of size irregularity constitute a linear function of the cell's position (as shown by the black line in Figure 5(a)) and can be fitted as follows:

$$R_i(x) = k \cdot x/w_0 + h_0 \tag{7}$$

where k and h_0 are the fitting parameters. The gradient parameter k is defined as the slope of the fitting linear function (as shown in Eq. (7)) of the spatial distribution of size irregularity. As shown in Figure 5(a), though the relationship between the size irregularity and x is non–linear in the low x/w_0 regions, its trend is linear in the whole research range.

The following steps of a simplified method was proposed to analyze the spatial distribution of size irregularity: (1) divide the model into a sufficient number of slices along the gradient direction, (2) calculate the mean size irregularity of each slice, and (3) analyze the relationship between the mean values of the size irregularity and positions. For

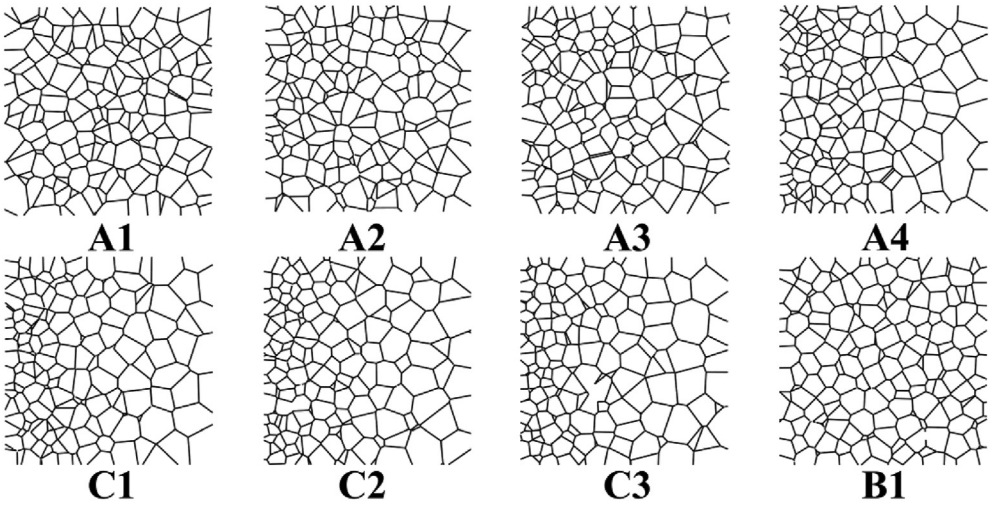

Figure 2. $Y = 0$ cross-sectional structures of the gradient 3D Voronoi models.

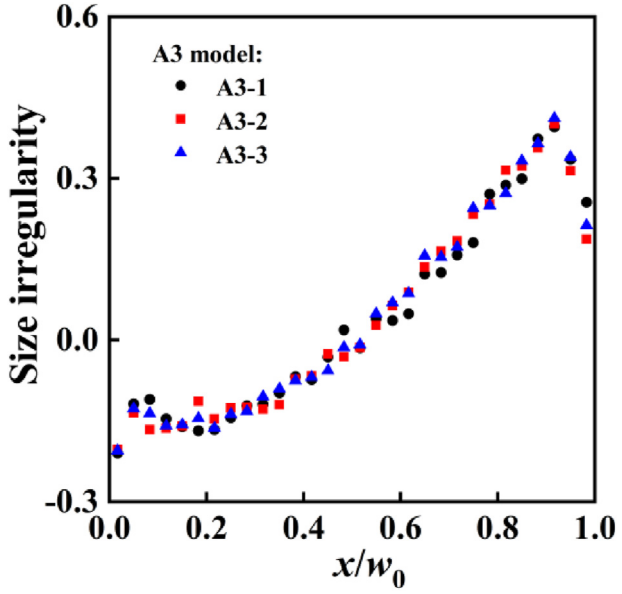

Figure 3. Repeatability of the proposed method for constructing the gradient 3D Voronoi model.

example, the C3 model can be divided into 30 slices with a length of 1 mm, and the relationship between the mean value of the size irregularity (the red scatters) and position is illustrated by the red dotted line in Figure 5(a). The red dotted line nearly coincides with the black line, which indicates that the simplified method is effective for examining the spatial distribution of the size irregularity of the 3D Voronoi model.

The spatial distributions of size irregularity in the gradient direction of the 3D Voronoi models with different modeling parameters are shown in Figure 5(b) and (c). The model data of each SIGMF could be well fitted by a linear function (Eq. (7)) in $x/w_0 \in [0.05, 0.92]$. The data near the boundary should be removed because the cells near the boundary were cut and incomplete. The gradient parameter k of each model is obtained and listed in Table 1, and it significantly varies with either the modeling parameter a or b. It should be noted that the defined gradient parameter $k \neq a/w_0$. The spatial distribution of size irregularity in non-gradient directions (y- or z-direction) was an approximately flat and straight line (as shown in Figure 5(d)). This indicates a uniform distribution of size irregularity in the non-gradient directions.

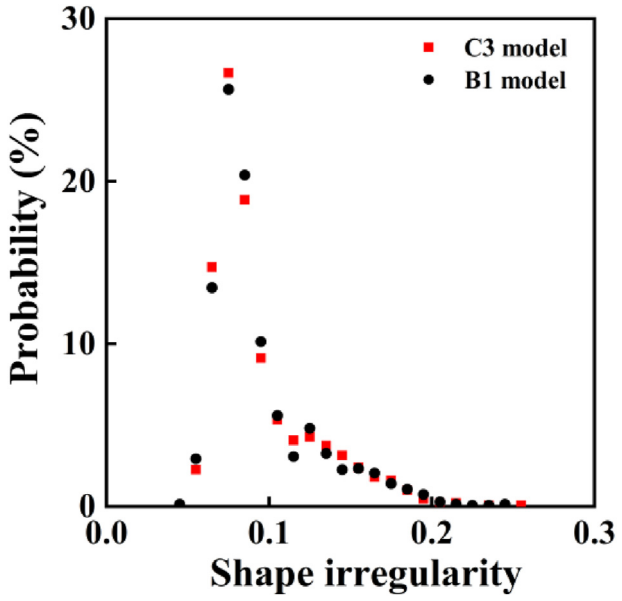

Figure 4. Probability of shape irregularity for the C3 and B1 models.

2.2.2. Spatial distribution of relative density

The SIGMFs have a nonlinear spatial distribution of relative density, as shown in Figure 6(a). The relationship of the relative density ρ_f with the cell diameter d and thickness t is determined to as follows based on Gibson and Ashby [1]:

$$\rho_f = h_1 \cdot \frac{t}{d} \tag{8}$$

where h_1 is a constant. Combining Eqs. (1), (7), and (8), for the SIGMFs, the relative density can be expressed using k as follows:

$$\rho_f(x) = h_1 \cdot \frac{t}{k \cdot x/w_0 \cdot d_0 + h_2} \tag{9}$$

where h_1 and h_2 are the fitting constants. This analytical function well characterizes the spatial distribution of relative density of the SIGMF, e.g., the data of the C3 model with an average relative density $\bar{\rho}_f = 14\%$ shown in Figure 6(b). The solid red line presents the theoretical values of Eq. (9) and the fitting values of h_1 and h_2 were 3.02, 1.82, respectively. The data near the boundaries are smaller than those predicted by theoretical function because the cells near boundaries were cut and incomplete, and the data could be fitted well by linear functions shown by the blue dotted lines in Figure 6(b).

2.3. Uniaxial compression finite element model

The size irregularity gradient 3D Voronoi foams were meshed using the finite-element meshing tool after appropriate pruning. A set of recommended dimensionless modeling and computing parameters [46] was used to ensure better simulation efficiency and accuracy. The 3D Voronoi model was meshed using shell elements with a size of 0.13 mm (as shown in Figure 7(a)). The total number of elements was approximately 1600000. ABAQUS/Explicit dynamic analysis was employed to simulate quasi-static uniaxial compression tests. The finite element model is illustrated in Figure 7(b). A pair of rigid bodies was added at the top and bottom of the 3D Voronoi foam. One was fixed, and the other was compressed with a constant velocity $v = 15$ mm/s (strain rate $\dot{\varepsilon} = 0.5$ /s). The foams had an equal average relative density of 14%. The mechanical properties of the matrix material (aluminum) [40] are employed to perform the response of a metal foam. The values of the density, elastic modulus, Poisson's ratio, yield stress, and tangent modulus are 2700 kg/m^3, 70 GPa, 0.33, 80 MPa, and 30 MPa, respectively [40]. Ductile damage and shear damage are used to describe the damage and failure properties of the matrix metal material (aluminum).

The rationality of the finite element model has been verified by performing uniaxial compression, uniaxial tension, and biaxial tension experiments on aluminum foams with random cells [40, 47, 48]. The following criteria should be satisfied to ensure the rationality of quasi-static simulation: the ratio d_1 of artificial strain energy to internal energy should be at most 10%, and the ratio d_2 of kinetic energy to internal energy should be less than 5%. These were satisfied for the size irregularity gradient 3D Voronoi foams (see Figure 8(a) and (b)). Therefore, the simulation results for the size irregularity gradient 3D Voronoi foams are reasonable.

3. Results

3.1. Comparisons of compressive properties of SIGMF and cell wall gradient metal foam

The nominal stress and strain are defined as follows:

$$\bar{\sigma} = \frac{F_p + F_f}{2S_0}; \bar{\varepsilon} = \frac{\Delta l}{w_0} \tag{10}$$

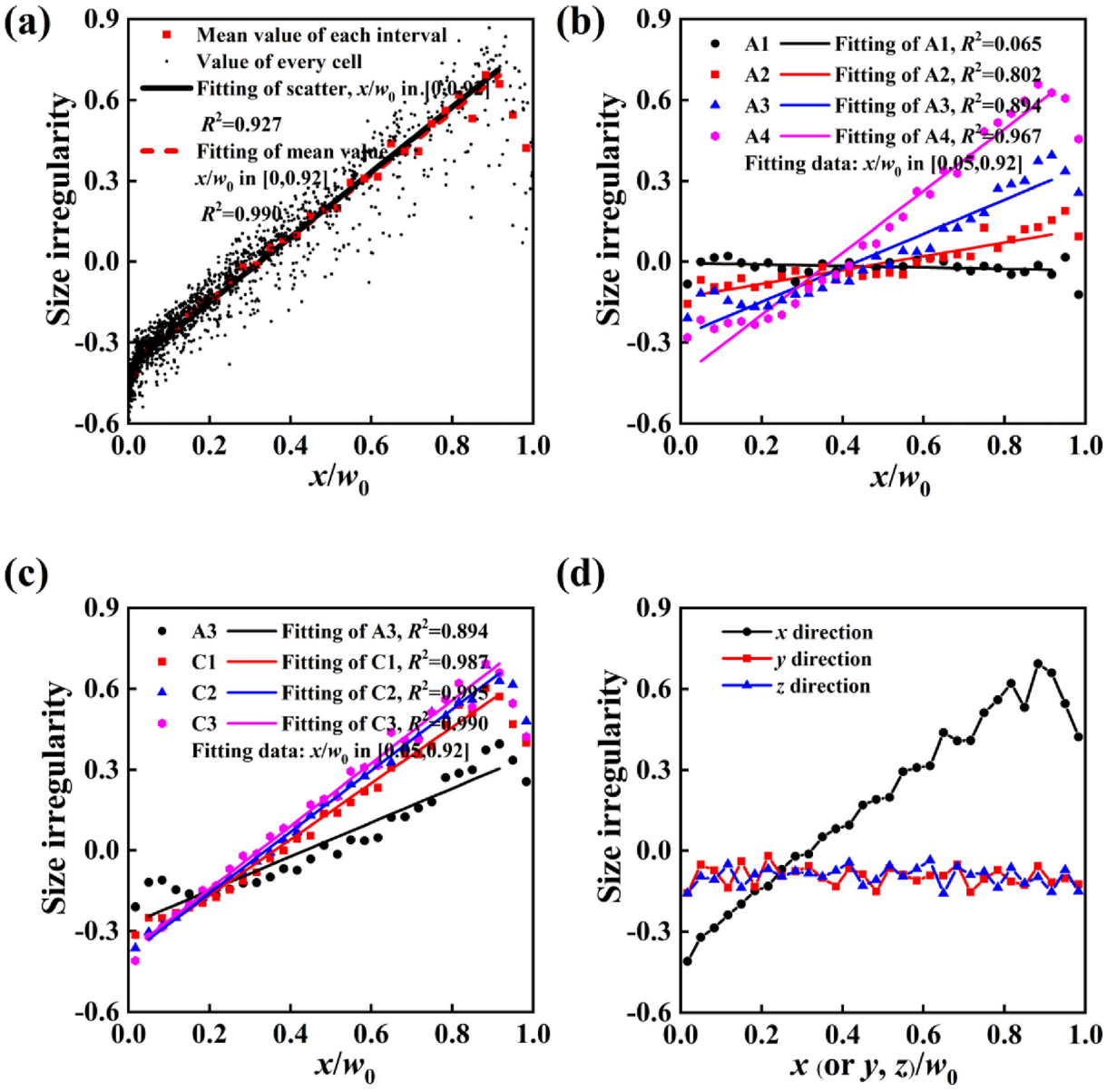

Figure 5. Linear fittings of the spatial distributions of the size irregularity for (a) C3 model in x direction, (b) A1∼A4 models with a ranging from 0 to 4 mm and b being constant zero, (c) models with increase of b from 0 to 1.3 mm and a being constant 3 mm; (d) spatial distribution of C3 model in different directions.

where p and f represent the loading rigid body and fixed rigid body, respectively. $S_0 = w_0^2$ is the area of a cubic 3D Voronoi with a length of w_0, and Δl is the displacement of the loading rigid body along the compressive direction.

Nominal stress–strain curves of the C3 and B1T models with average relative densities ranging from 8% to 30% are shown in Figure 9(a) and (b). Significant differences are observed. These become more significant as the average relative density increases. The SIGMF has both a larger first peak stress and longer strain-hardening region than the cell wall gradient foam with an equal relative density gradient. In general, if the nominal strain is marginal, the stress of the SIGMF can be smaller than that of the cell wall gradient foam. However, the stress of the SIGMF is significantly higher if the nominal strain is sufficiently high.

The energy absorptions of these two gradient foams are shown in Figure 9(c) and (d). The SIGMF absorbs less energy than the cell wall gradient foam when $\bar{\varepsilon} < 0.9$. Consequently, it would overestimate the energy absorption capacity of the SIGMF when it is considered to be identical to the cell wall gradient foam.

Deformations of the C3 and B1T models with an equal average relative density of 14% are compared in Figure 10. These two gradient foams were compressed layer-by-layer from the large cells to the small cells before densification. However, the deformation region of the SIGMF was smaller than that of the cell wall gradient foam. This is consistent with the experimental observation of Duan et al. [11].

Therefore, the density gradient is insufficient to characterize the mechanical properties of gradient foams because of the significant differences in the stress–strain curve, energy absorption, and deformations. Considering that the spatial distribution of relative density can be expressed by the gradient parameter of size irregularity (as shown in Eq. (9)), the gradient parameter of size irregularity (rather than relative density) could be more effective for characterizing the macro-compressive properties of SIGMFs.

3.2. Effects of size gradient parameter on stress–strain curves and energy absorptions

The stress–strain curves of the SIGMFs are shown in Figure 11. The stress–strain curve can be divided into five stages: elastic, stress decline, strain hardening, plateau, and densification. The SIGMF had a large strain variation range from the beginning of condensation to its

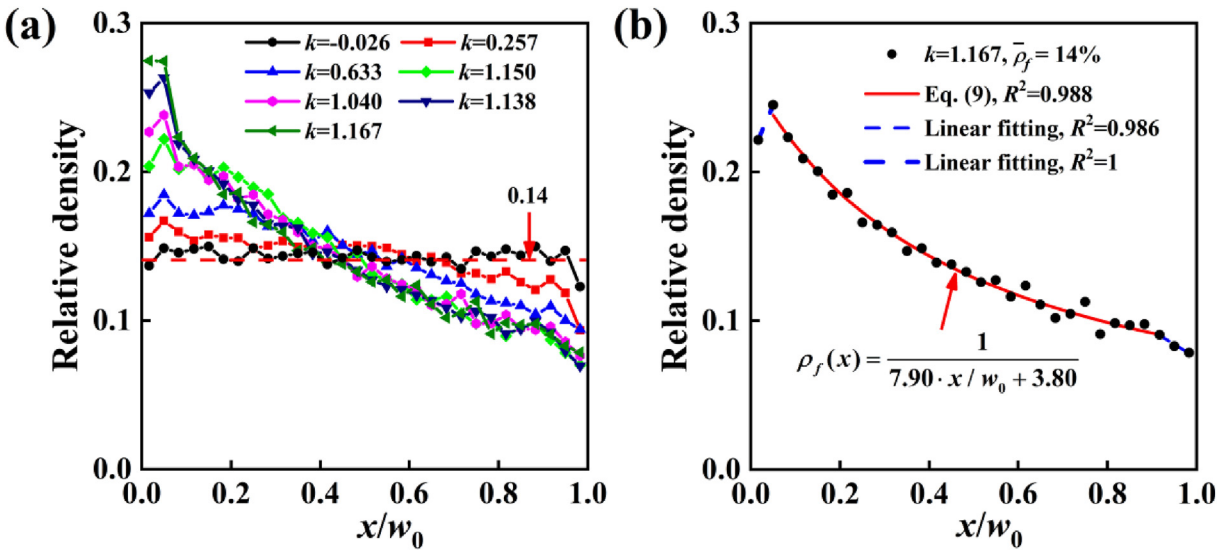

Figure 6. Spatial distributions of the relative density: (a) spatial distributions of the relative density for foams with different values of the gradient parameter *k*; (b) fitting of the spatial distribution of the relative density for C3 model by the theoretical equation.

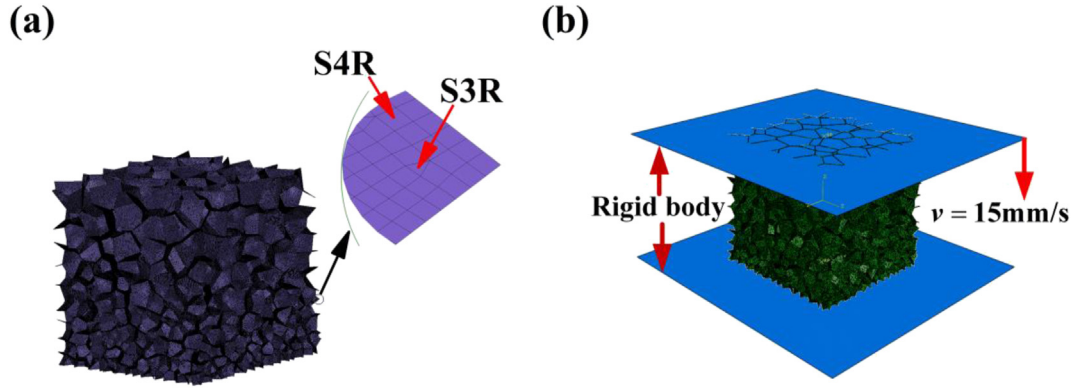

Figure 7. Uniaxial compression finite element model: (a) meshed elements; (b) finite element model.

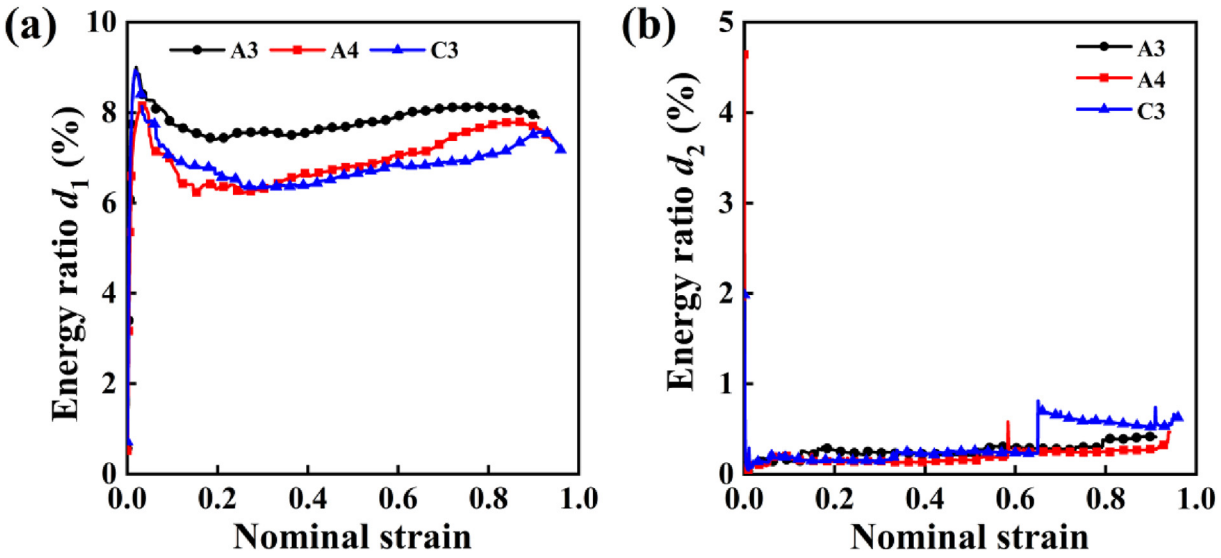

Figure 8. Energy ratios of simulations for gradient 3D Voronoi models under quasi-static compression loading: (a) the ratio of artificial strain energy to internal energy for models; (b) the ratio of kinetic energy to internal energy for models.

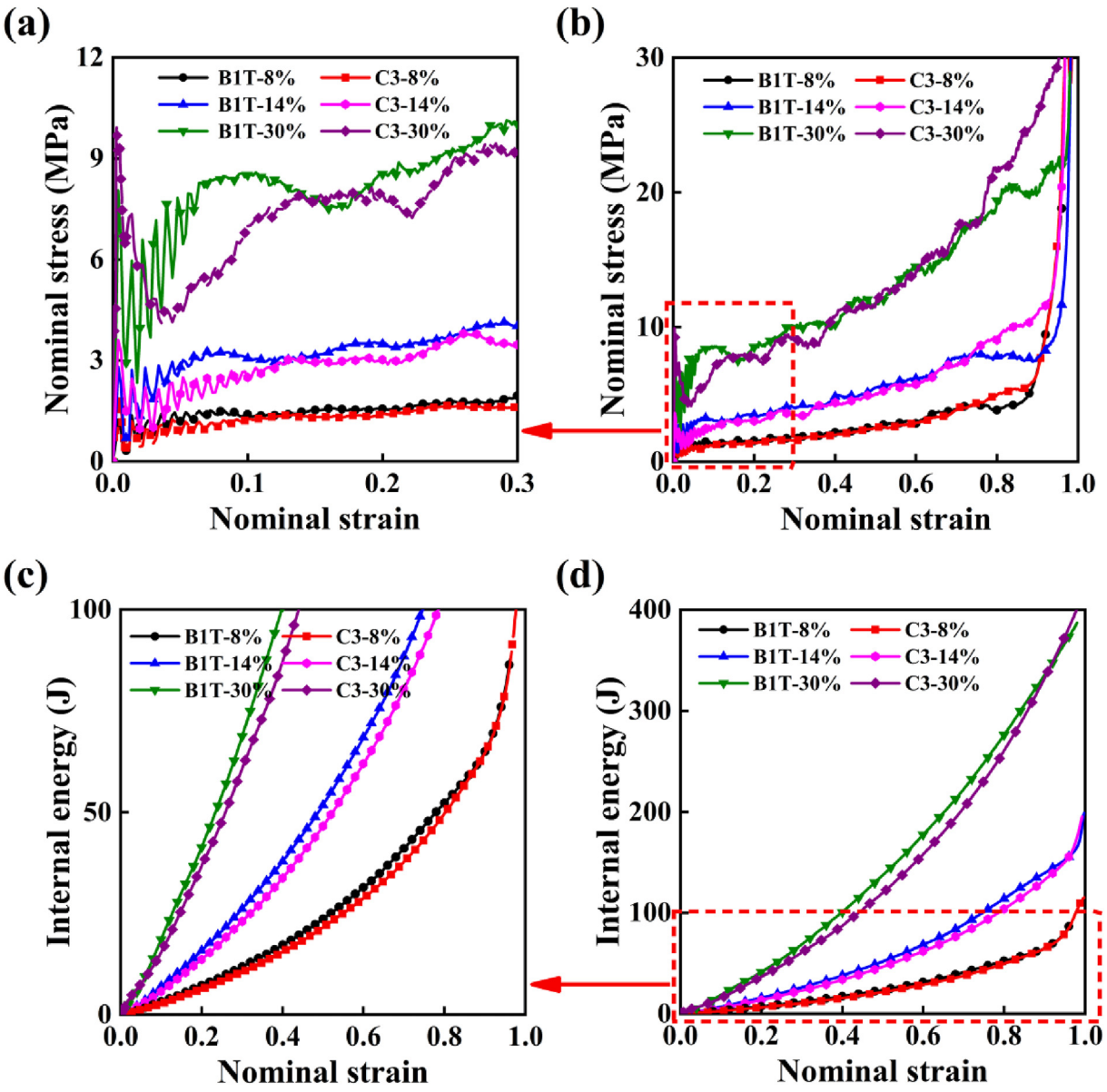

Figure 9. Comparisons of compressive properties between the C3 and B1T models: (a) stress–strain curve, strain ranging from 0 to 0.3; (b) stress–strain curve, strain ranging from 0 to 1; (c) internal energy ranging from 0 to 100 J; (d) internal energy ranging from 0 to 400 J.

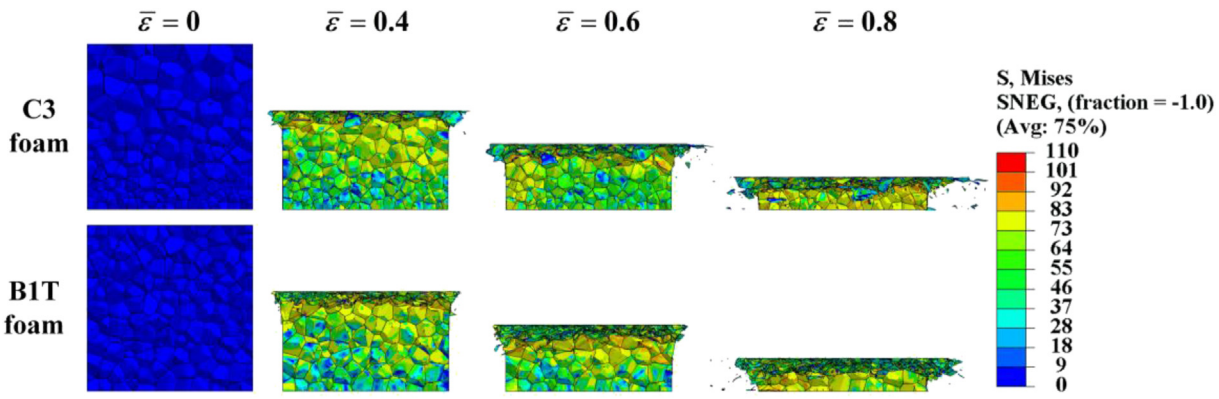

Figure 10. Compression deformations of the C3 and B1T models in the front viewport.

completion. This was consistent with the experimental results of gradient foams [12, 16, 33]. The strain-hardening range plays a crucial role in the macroscopic compressive properties of SIGMFs.

The strain-hardening range becomes longer as the gradient parameter k increases, and the stress plateau range shortens or even disappears as shown in Figure 11. Meanwhile, the slope of the stress–strain curve in the elastic range is independent of k (as shown in Figure 11(a)). This may be because all cells of gradient foams deform slightly under compression in the elastic range. Such slight differences in localized deformation would not result in an apparent difference in the macroscopic mechanical response. If the gradient foams have the same relative density and the same mean diameters of cells, though they possess different k, they still have similar stress–strain curves in the elastic region. This result agrees with the experimental results of Duan et al. [16].

The internal energy–strain diagrams of the SIGMFs are shown in Figure 12(a). The gradient parameter significantly affected the internal energy. When the strain was marginal ($\bar{\varepsilon} < 0.2$), the larger the gradient parameter k of the foam, the lower was the internal energy absorbed by the foam. However, when the strain was large ($\bar{\varepsilon} > 0.6$), the foam with a larger k absorbed more internal energy. Therefore, superior energy absorption of gradient foams is realized under large deformations.

Miltz and Gruenbaum [49] proposed a parameter called energy absorption efficiency η (see Eq. (11)) to evaluate the energy absorption of foams, which is expressed as follows:

$$\eta = \frac{1}{\sigma_m} \int_0^{\varepsilon_m} \sigma d\varepsilon \tag{11}$$

where ε_m and σ_m are the strain and stress, respectively, at any instant. The optimal energy absorption occurs when the efficiency attains its maximum value.

The efficiency–strain curves of the SIGMFs are shown in Figure 12(b). The dotted lines represent the instant at which the efficiency attains the maximum value. The maximum value of η decreases as k increases. This is because the gradient foam with larger k exhibits a more obvious strain hardening behavior as shown in Figure 11(b), and the energy absorption efficiency would decrease with strain hardening behavior of metal foams during compression.

For metal foams, the densification strain ε_D could be commonly defined as the corresponding strain when the energy efficiency attains its maximum value. The densification strain for each stress–strain curve of gradient foams was marked using a solid red star and shown in Figure 11(b). These densification strain increases generally with the increase of k, as shown in Figure 13. And the model A1 and A4 exhibits unnormal values, which may be because when the stress–strain curves of gradient foams exhibit obvious stress fluctuations at large nominal strain, the defined densification strain of a gradient foam may be far away from the real densification point.

3.3. Deformation analysis of SIGMF

The compressive deformation of the C3 model is shown in Figure 10. Two typical deformation modes appeared gradually as the displacement increases: (I) in the beginning, structures were compressed layer-by-layer from the larger cells to the smaller ones; and (II) in the densification range, the remaining structures were deformed more and more uniformly (similar to uniform Voronoi foams).

To measure the localized deformation of SIGMFs, the localized strain of any i-th slice can be defined as follows:

$$\varepsilon_i = 1 - \frac{x_i^j - x_{i-1}^j}{x_i^0 - x_{i-1}^0} \tag{12}$$

where i is the number of slices (see Figure 14(a)), $i = 1$ is the slice with the smallest irregularity, j is the specific instant, and $j = 0$ is the initial instant. x_{i-1}^j, x_i^j are the coordinates of the left and right boundaries, respectively, of the i-th slice in the x-direction at the instant j. The localized strain can be used to quantitatively analyze the deformation mechanisms.

The localized strain of each slice for the C3 model is shown in Figure 14(b). The localized strain first began at larger cells and was transmitted layer-by-layer to smaller cells in the strain-hardening range as the number of slices decreased from 15 to 1 (see Figure 14(b)). The localized strain of each slice increased abruptly and then, remained flat. This implies that local structures deformed intensively, and then these structures could be assumed to be completely in translational motion when the localized strain reached a critical value. The critical value of each slice was nearly equal (approximately 0.9, see Figure 14(b)), and it was larger than the densification strain of most uniform foams. Therefore, it is inaccurate to replace the stress of the local structures of the SIGMF with the plateau stress of the uniform foam.

To evaluate the localized deformation of each slice, t_i^{int}, t_i^{pla} were defined as the earliest instant at which the localized strain of the i-th slice begins to increase abruptly and maintains plate lines, respectively (e.g.,

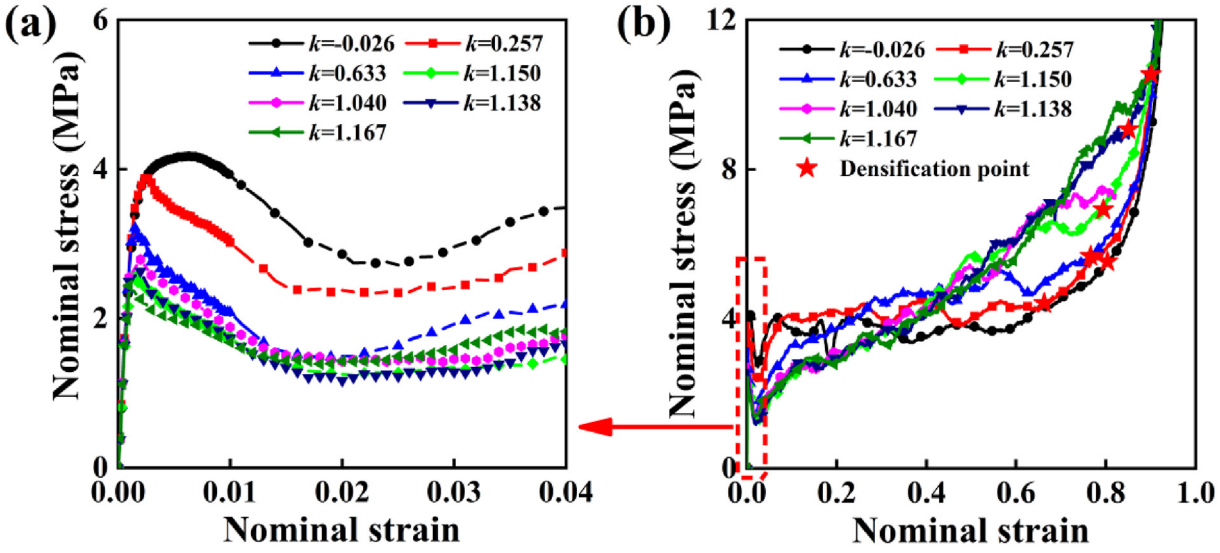

Figure 11. Compressive stress–strain curves of metal foams with different values of gradient parameter: (a) strain ranging from 0 to 0.04; (b) strain ranging from 0 to 1.

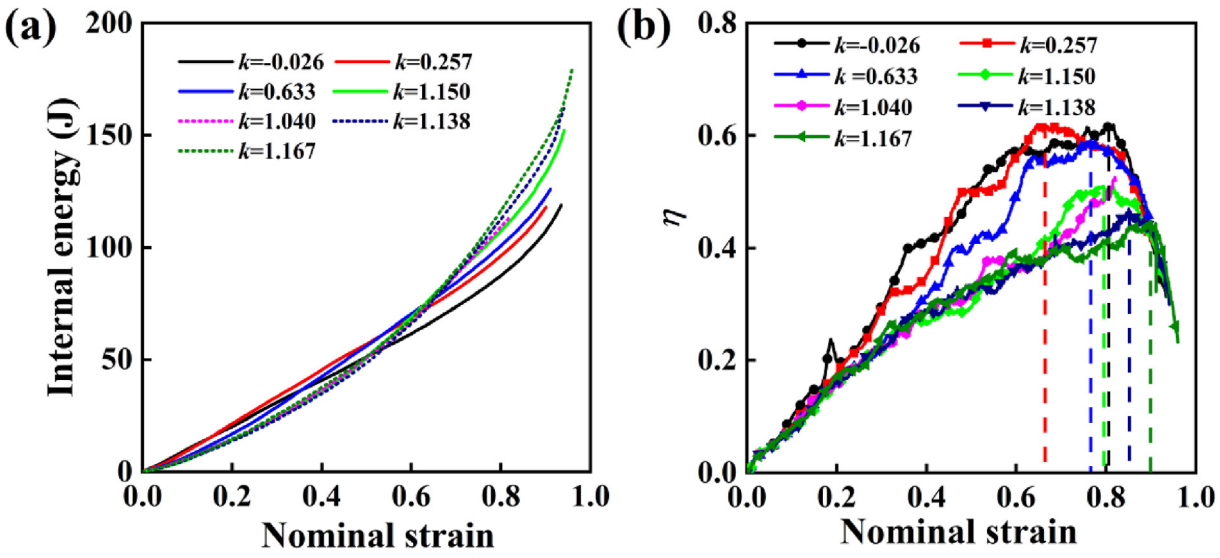

Figure 12. Effects of gradient parameter on (a) internal energy and (b) energy efficiency.

big blue dots for the eighth slice shown in Figure 14(b)). The deformation region was larger than one slice and smaller than two slices because $t_{i+2}^{\text{int}} > t_i^{\text{pla}} > t_{i+1}^{\text{int}}$. Three time-increments were defined below: $\Delta t^{\text{p-i}} = t_i^{\text{pla}} - t_i^{\text{int}}; \Delta t^{\text{p-p}} = t_{i+1}^{\text{pla}} - t_i^{\text{pla}}; \Delta t^{\text{i-i}} = t_{i+1}^{\text{int}} - t_i^{\text{int}}$, and they were compared to the characterized time increment $\Delta t_{\text{cha}} = w_0/15/v = 0.133$ s as shown in Figure 14(c). Three observations could be obtained: (1) $\Delta t^{\text{p-i}} > \Delta t_{\text{cha}}$, therefore the deformation region should be divided into three parts (the large plastic deformation region named A, represented by the pink block A in Figure 14(b) and red dot block in Figure 14(d); the small plastic deformation region named B, represented by the pink dot block B in Figure 14(b) and blue dot block in Figure 14(d); and the nearly undeformed region, represented by the part excluding regions A and B in Figure 14(d)). (2) Region A dominates the structure's deformation in the strain-hardening region. Therefore, it is rational to assume that the deformation occurred only in a small finite domain near the analytical rigid body. Furthermore, the relationship between the nominal strain $\bar{\varepsilon}$ and position x of cells in the strain-hardening range can be simplified as follows.

$$\bar{\varepsilon} = 1 - x/w_0 \tag{13}$$

(3) The width l_{B0} of region B does not vary because both $\Delta t^{\text{p-p}}$ and $\Delta t^{\text{i-i}}$ are nearly constant during compression (see Figure 14(c)).

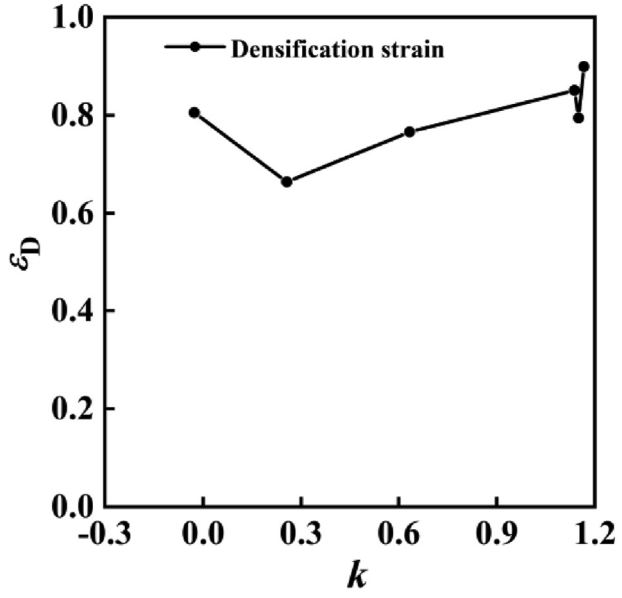

Figure 13. Effects of gradient parameter on the densification strain of size irregularity gradient metal foams.

4. Constitutive model of the stress–strain curve of SIGMF

4.1. Establishment of theoretical model

A typical five-stage characterization is observed for the stress–strain curve of SIGMF (see Figure 11), so all of these characterizations should be described by constitutive model. Among these five stages, the strain-hardening range plays a crucial role in the macroscopic compressive properties of SIGMFs. Therefore, we construct a theoretical model with only the parameters of the size irregularity gradient to characterize the macroscopic responses of the SIGMF in the strain-hardening range. The theoretical model was established based on the energy conservation law and the layer-by-layer deformation model.

Given the condition that the kinetic energy of foam structures can be omitted under quasi-static compression, the external work W should be equal to the internal energy E based on the energy conservation law. The power of the external work P can be expressed as follows.

$$P = \frac{\mathrm{d}E}{\mathrm{d}t} \tag{14}$$

The power when the foam is compressed with a constant velocity v can be determined as

$$\mathrm{d}P = \mathrm{d}(F \cdot v) = \mathrm{d}F \cdot v \tag{15}$$

Here, F is the external force in the compression direction. According to Newton's third law, it should be equal to the reaction force of rigid bodies in the compression direction under quasi-static compression.

The stress contours of the C3 model are shown in Figure 14(d). At any time t_0 during deformation mode (I), the deformation of foams can be divided into three parts (named A, B, and C; see Figure 14(b) and (d)). Comparing the deformations at the instant $t = t_0$ with those at $t = t_0 + \Delta t$, the following five assumptions could be rational to describe the deformation of structures during a time increment Δt: (1) The structures in region A would not deform further and could be assumed could be

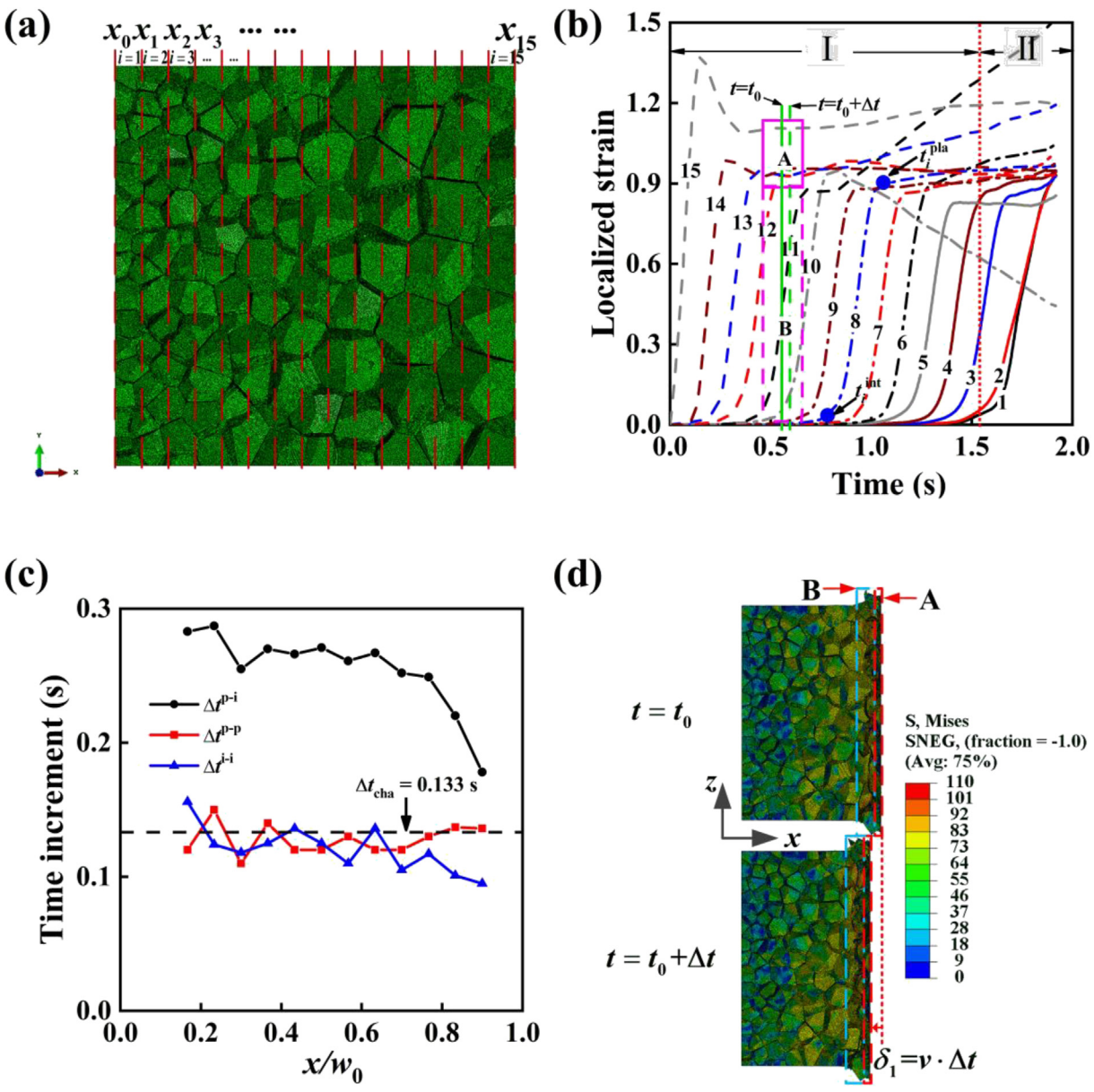

Figure 14. Deformation analysis of the C3 model: (a) divided the foam into slices in x direction; (b) localized strain of each slice under compression; (c) three time-increments of localized strain for each slice; (d) deformation process of the C3 model under compression with increase of time, red dot line region named A represents the large plastic deformation region, blue dot line region named B represents the small plastic deformation region.

assumed to be completely in translational motion. (2) The structures on the right side of region B at $t = t_0$ within a distance $\delta_1 = v \cdot \Delta t$ deformed from nearly zero to a large strain (similar to the case of region A). (3) Both the deformation degree of matrix structures in region B and the width of region B would not vary. However, the structures of region B transformed as the position of the region B shifted. (4) The deformation energy of the structures in region C could be omitted. (5) Region A dominated the deformation in the strain-hardening region.

The increment of deformation energy can be determined based on the assumption (4), as following:

$$\Delta E = (\overline{\omega}_{A1} \cdot V_{sA1} + \overline{\omega}_{B1} \cdot V_{sB1}) - (\overline{\omega}_{A0} \cdot V_{sA0} + \overline{\omega}_{B0} \cdot V_{sB0}) \tag{16}$$

where the subscripts 0 and 1 represent the instants $t = t_0$ and $t = t_0 + \Delta t$, respectively; $\overline{\omega}$ is the equivalent mean energy density of the matrix material in the deformed region; V_{sA}, V_{sB} are the volumes of the metal matrix material in regions A and B, respectively.

The localized strains in the plate straight line were approximately equal for each slice (see Figure 14(b)). Thus, $\overline{\omega}_{A1} = \overline{\omega}_{A0}$. Considering assumption (3), $\overline{\omega}_{B1} = \overline{\omega}_{B0}$. Combining assumptions (1) and (2), we obtain

$$\Delta E = \overline{\omega}_{A0} \cdot \rho_{fB0} \cdot v \cdot \Delta t \cdot S_0 + \overline{\omega}_{B0} \cdot (\rho_{fB1} - \rho_{fB0}) \cdot V_{B0} \tag{17}$$

where ρ_{fB0}, ρ_{fB1} are the relative density of deformation region B at $t = t_0$ and $t = t_0 + \Delta t$, respectively; area $S_0 = w_0^2$; and $V_{B0} = l_{B0} \cdot S_0$ is the foam volume of deformation region B. l_{B0} is the width of region B in the compressive direction at $t = t_0$. It does not vary according to assumption (3). When $\Delta t \to 0$,

$$dE = \overline{\omega}_{A0} \cdot \rho_{fB0} \cdot v \cdot S_0 \cdot dt + \overline{\omega}_{B0} \cdot \frac{d\rho_{fB}}{dx} \cdot v \cdot l_{B0} \cdot S_0 \cdot dt \tag{18}$$

The nominal stress can then be defined as

$$d\bar{\sigma} = \frac{dF}{S_0} \tag{19}$$

Combining Eqs. (14), (15), (18), and (19) yields the relationship between the nominal stress and relative density.

$$d\bar{\sigma} = \bar{\omega}_A \cdot d\rho_{fB} + \bar{\omega}_B \cdot l_{B0} \cdot d\left(\frac{d\rho_{fB}}{dx}\right) \tag{20}$$

According to assumption (5), the localized strain in Figure 14(b), the stress contour in Figure 14(d), and the spatial distribution of relative density in Figure 6(a), the second part of Eq. (20) can be omitted if it is significantly smaller than the first part. Therefore, Eq. (20) can be simplified as

$$d\bar{\sigma} = \bar{\omega}_A \cdot d\rho_{fB} \tag{21}$$

Eq. (21) indicates that the nominal stress is a linear function, rather than a complex exponential function [16], of the current relative density. This conclusion is verified by the simulation results of the C3 model in the strain-hardening range ($\bar{\varepsilon} \in [0.015, 0.77]$) shown in Figure 15(a), and the experimental results shown in Figure 15(c). Here, $\bar{\omega}_A$ is the equivalent mean energy density of the matrix material in a large-deformation region.

Substituting Eqs. (9) and (13) into Eq. (21), the relationship between the nominal strain and nominal stress in the strain-hardening region can be expressed as follows:

$$\bar{\sigma} = \bar{\omega}_A \cdot \frac{h_1 t}{k \cdot (1 - \bar{\varepsilon}) \cdot d_0 + h_2} + \bar{\sigma}_1 \tag{22}$$

where $\bar{\omega}_A$ is the equivalent mean energy density; k is the gradient parameter of size irregularity; d_0 is the mean equivalent diameter; t is the thickness of cells; $h_1, h_2, \bar{\sigma}_1$ are fitting constants.

The stress–strain relationship was linear in both elastic and stress-decline stages. The function Eq. (23) proposed by Zheng et al. [50] can

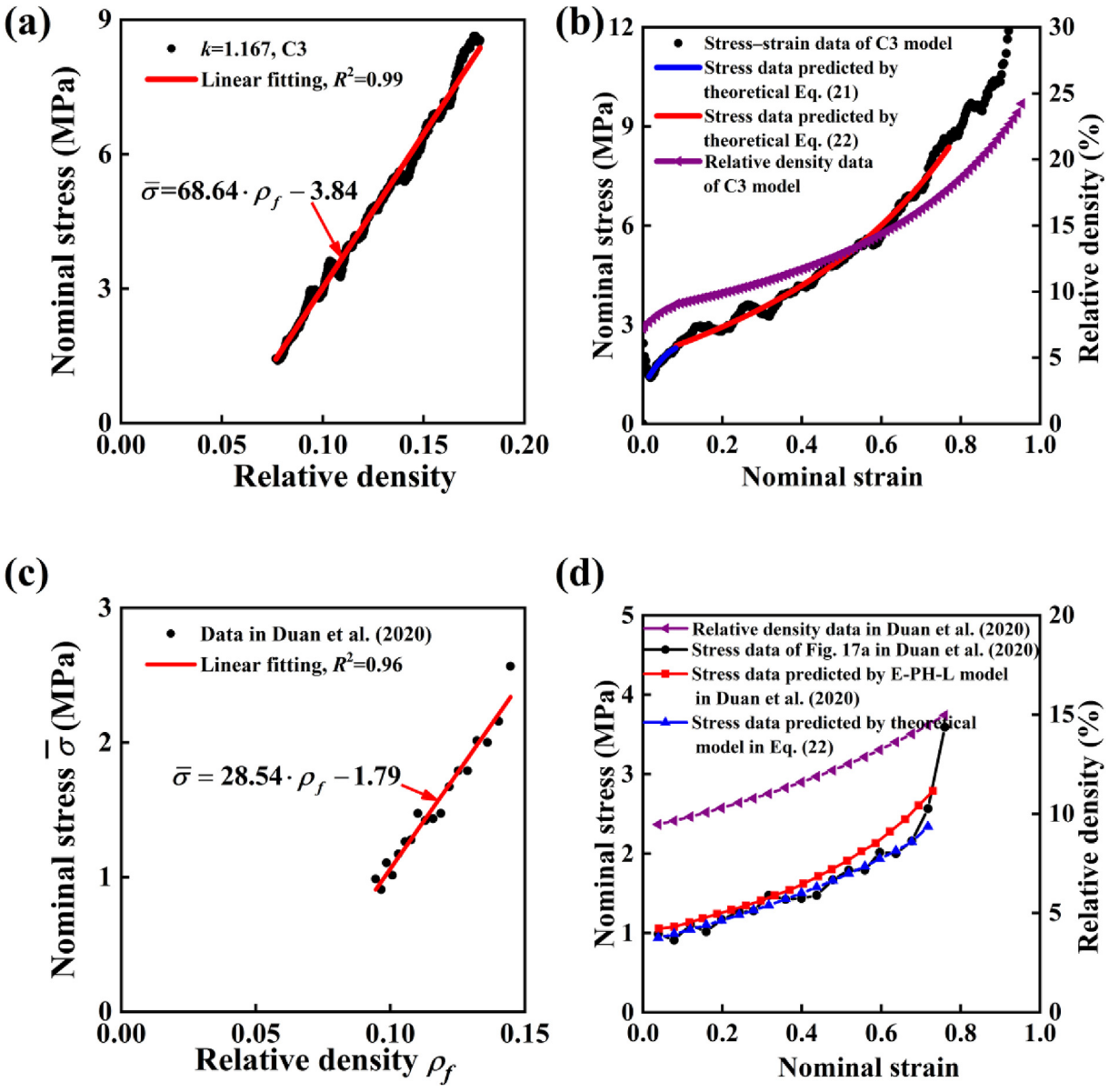

Figure 15. Verification of the theoretical model by simulation and previous experimental results in strain-hardening range: (a) relationship between nominal stress and relative density of the C3 model; (b) comparison of theoretical predictions with simulation results of the C3 model; (c) relationship between nominal stress and relative density of published experimental results by Duan et al. (2020); (d) comparison of theoretical predictions with published experimental results by Duan et al. (2020).

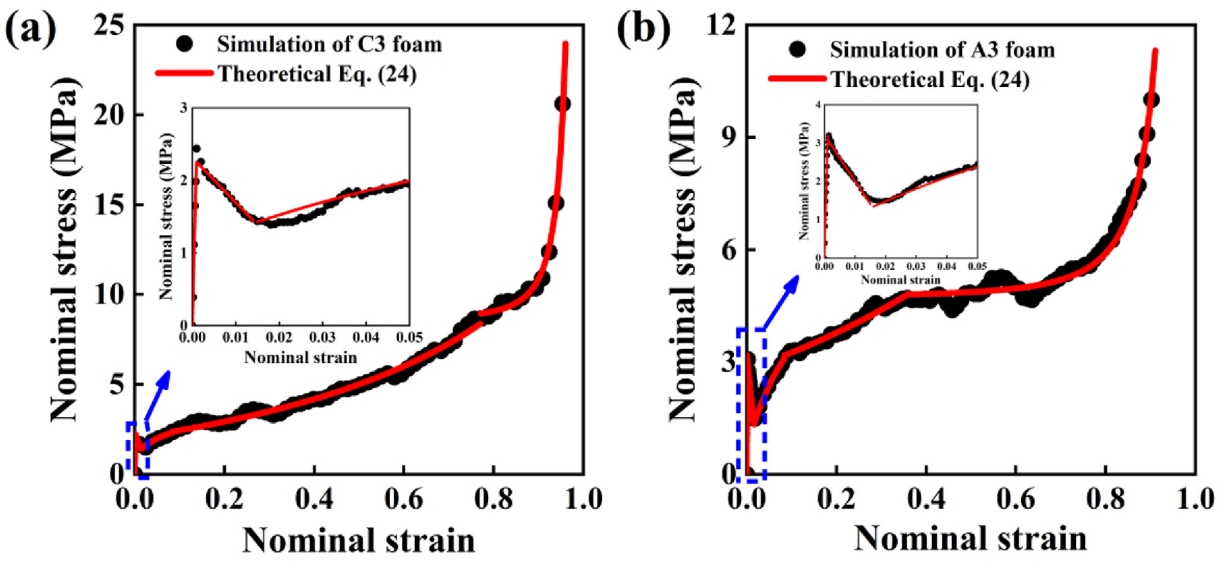

Figure 16. Characterizations of the stress–strain curve for (a) C3 model; (b) A3 model.

be employed to effectively describe the plateau and densification ranges of gradient foams:

$$\overline{\sigma} = \overline{\sigma}_0 + c \cdot \frac{\overline{\varepsilon}}{(1-\overline{\varepsilon})^2} \tag{23}$$

where $\overline{\sigma}_0$ and c are the fitting parameters that depend on the relative density. Therefore, the segmented function Eq. (24) can be employed to describe all the five stages of the stress–strain curve.

$$\overline{\sigma} = \begin{cases} c_1\overline{\varepsilon} \quad (\overline{\varepsilon} \le \overline{\varepsilon}_1) \\ c_2 + c_3\overline{\varepsilon} \ (\overline{\varepsilon}_1 < \overline{\varepsilon} \le \overline{\varepsilon}_2) \\ \overline{\omega}_A \cdot \dfrac{c_4 \cdot t}{k \cdot (1-\overline{\varepsilon}) \cdot d_0 + c_5} + c_6 \ (\overline{\varepsilon}_2 < \overline{\varepsilon} < \overline{\varepsilon}_3) \\ c_7 + c_8 \dfrac{\overline{\varepsilon}}{(1-\overline{\varepsilon})^2} \quad (\overline{\varepsilon} \ge \overline{\varepsilon}_3) \end{cases} \tag{24}$$

Here $c_i (i = 1, 2, \ldots, 8)$ is the fitting parameters; c_1 is the elastic modulus in the elastic region; c_4, c_5 are the fitting parameters of relative density; c_7 is the plateau stress; d_0 is the mean equivalent diameter; t is the thickness of gradient foams; $\overline{\varepsilon}_1$ is the strain at the instant the first peak stress appears; $\overline{\varepsilon}_2$ is the strain at the instant the first valley appears; $\overline{\varepsilon}_3$ is the strain at the beginning of the plateau stage.

4.2. Verification of theoretical model

The theoretical model in Eq. (22) is in good agreement with the simulation results in the strain-hardening region, as shown in Figure 15(b). The nominal stress exhibits linear function (Eq. (21)) of the relative density in strain-hardening region, including the stress–strain curve at the beginning of the strain-hardening region where the theoretical Eq. (9) could not well describe the spatial distribution of relative density. When the linear function well characterizes the spatial distribution of relative density near the boundary (as blue dot lines shown in Figure 6(b)), combining Eq. (21), the stress could be well predicted as shown by the blue line in Figure 15(b). Therefore, the theoretical model is in good agreement with the simulation results.

This theoretical model shows well agreement with experimental results of the gradient foam named "M1-PG" (reported in Duan et al. [16]), as shown in Figure 15(d). The spatial distribution of the relative density of "M1-PG" foam can be determined using Eq. (8) proposed by Gibson and Ashby [1]with the foam's modeling parameters ($C = 2.32$, $t = 0.4$ mm, $S_{max} = 10$ mm, $S_{min} = 5$ mm, $M = 1$) [16]. The relationship between the nominal stress and relative density can be well fitted by a linear function, as shown in Figure 15(c). This demonstrates that the proposed theoretical model in Eq. (21) is accurate. The predictions of the experimental stress–strain curve in the strain-hardening (nominal strain ranging from 0.04 to 0.72) by our theoretical model and E-PH-L model were shown in Figure 15(b). The coefficient of determinations of our theoretical model and the E-PH-L model are 0.97 and 0.95, respectively. These results indicated that our theoretical model better characterized the stress–strain curve in the strain-hardening than the E-PH-L model (see Figure 15(d). Meanwhile, the constitutive model proposed in Eq. (24) can accurately predict the simulation results for both C3 model with a large k (see Figure 16(a)) and A3 model with a small k (see Figure 16(b)). The fitting parameters are listed in Table 2. Thus, the proposed constitutive model can effectively characterize the macro quasi-static compressive mechanical properties of SIGMFs.

5. Conclusions

A series of metal foam models was developed using the 3D Voronoi technique. These have the same average relative densities, the same average equivalent diameters and different size irregularity gradients. The compression process of cell wall gradient metal foams and size irregularity gradient metal foams were studied carefully, respectively. The simulation results showed that there is obvious difference in macroscopic mechanical properties though these metal foams models have the same relative density gradient. The density gradient is insufficient to describe the macroscopic properties of gradient foams when the mesostructures become complex. The size irregularity gradient should be introduced to

Table 2. Fitting parameters of Eq. (24) for size irregularity gradient foams.

Model	c_1 (MPa)	c_2 (MPa)	c_3 (MPa)	$\overline{\omega}_A$ (MPa)	c_4	c_5 (mm)	c_6 (MPa)	c_7 (MPa)	c_8 (MPa)
C3	2502.40	2.32	−61.96	68.64	3.02	1.82	−3.84	8.62	0.03
A3	2884.80	3.21	−119.98	73.82	1.92	1.05	−3.67	4.75	0.06

characterize the macroscopic compressive properties of the SIGMFs. The structures of SIGMF were compressed layer-by-layer from the larger cells to smaller ones in the strain-hardening range. And a theoretical model was developed to characterize the compression process from the first cell-collapse to the condensation, showing a linear relationship between the nominal stress and the current relative density. These findings can be a useful tool to guideline the design and applications of gradient metal foams.

Declarations

Author contribution statement

Xiaoyang Zhang: Conceived and designed the experiments; Performed the experiments; Analyzed and interpreted the data; Contributed reagents, materials, analysis tools or data; Wrote the paper.

Liqun Tang, Bao Yang: Conceived and designed the experiments; Analyzed and interpreted the data; Contributed reagents, materials, analysis tools or data; Wrote the paper.

Heping Hu, Shifeng Tan: Performed the experiments; Contributed reagents, materials, analysis tools or data.

Funding statement

Xiaoyang Zhang was supported by Young Scientists Fund [11902140], Special Foundation for Theoretical Physics Research Program of China [11747157], Natural Science Foundation of Hunan Province [2018JJ3425 & 18C0449].

Data availability statement

Data included in article/supplementary material/referenced in article.

Declaration of interests statement

The authors declare no competing interests.

Additional information

No additional information is available for this paper.

References

[1] L.J. Gibson, M.F. Ashby, Cellular Solids: Structure and Properties, Cambridge University Press, Cambridge, 1997.
[2] A. Baroutaji, M. Sajjia, A.-G. Olabi, On the crashworthiness performance of thin-walled energy absorbers: recent advances and future developments, Thin-Walled Struct. 118 (2017) 137–163.
[3] L.L. Hu, T.X. Yu, Dynamic crushing strength of hexagonal honeycombs, Int. J. Impact Eng. 37 (5) (2010) 467–474.
[4] B. Yang, L.Q. Tang, Y.P. Liu, Z.J. Liu, Z.Y. Jiang, D.N. Fang, Localized deformation in aluminium foam during middle speed Hopkinson bar impact tests, Mater. Sci. Eng. A-Struct. 560 (2013) 734–743.
[5] N. Movahedi, M. Vesenjak, I.V. Belova, G.E. Murch, T. Fiedler, Dynamic compression of functionally-graded metal syntactic foams, Compos. Struct. 261 (2021), 113308.
[6] S. Bloodworth-Race, R. Critchley, R. Hazael, A. Peare, T. Temple, Testing the blast response of foam inserts for helmets, Heliyon 7 (5) (2021), e06990.
[7] Y. Zhang, S.Y. He, J.G. Liu, W. Zhao, X.L. Gong, J. Yu, Density gradient tailoring of aluminum foam-filled tube, Compos. Struct. 220 (2019) 451–459.
[8] J.Q. Yu, L. Song, F. Chen, P. Fan, L. Sun, M.Q. Zhong, J.T. Yang, Preparation of polymer foams with a gradient of cell size: further exploring the nucleation effect of porous inorganic materials in polymer foaming, Mater. Today Commun. 9 (2016) 1–6.
[9] L.H. Yang, L. Sui, Y.L. Dong, X.Y. Li, F. Zi, Z.X. Zhang, S.J. Yang, J.S. Yang, L.Z. Wu, Quasi-static and dynamic behavior of sandwich panels with multilayer gradient lattice cores, Compos. Struct. 255 (2021), 112970.
[10] X.R. Liu, X.G. Tian, T.J. Lu, B. Liang, Sandwich plates with functionally graded metallic foam cores subjected to air blast loading, Int. J. Mech. Sci. 84 (2014) 61–72.
[11] Y. Duan, Y. Ding, Z.Y. Liu, N.D. Hou, X.H. Zhao, H.F. Liu, Z.Q. Zhao, B. Hou, Y.L. Li, Effects of cell size vs. cell-wall thickness gradients on compressive behavior of additively manufactured foams, Compos. Sci. Technol. 199 (2020), 108339.
[12] T. Fiedler, N. Movahedi, L. York, S. Broxtermann, Functionally-graded metallic syntactic foams produced via particle pre-compaction, Metals 10 (3) (2020) 314.
[13] S.Y. He, Y.N. Lv, S.T. Chen, G. Dai, J.G. Liu, M.K. Huo, Gradient regulation and compressive properties of density-graded aluminum foam, Mater. Sci. Eng. A-Struct. 772 (2020), 138658.
[14] H.F. Xi, L.Q. Tang, S.H. Luo, Y.P. Liu, Z.Y. Jiang, Z.J. Liu, A numerical study of temperature effect on the penetration of aluminum foam sandwich panels under impact, Compos. B Eng. 130 (2017) 217–229.
[15] J.Y. Chen, P. Zhang, Y.S. Cheng, J. Liu, On the crushing response of the functionally graded metallic foams based on 3D Voronoi model, Thin-Walled Struct. 157 (2020), 107085.
[16] Y. Duan, X.H. Zhao, B. Du, X.P. Shi, H. Zhao, B. Hou, Y.L. Li, Quasi-static compressive behavior and constitutive model of graded foams, Int. J. Mech. Sci. 177 (2020), 105603.
[17] X.H. Yu, Q.H. Qin, J.X. Zhang, S.Y. He, C.P. Xiang, M.S. Wang, T.J. Wang, Crushing and energy absorption of density-graded foam-filled square columns: experimental and theoretical investigations, Compos. Struct. 201 (2018) 423–433.
[18] Q. Gao, W.H. Liao, Energy absorption of thin walled tube filled with gradient auxetic structures-theory and simulation, Int. J. Mech. Sci. 201 (2021), 106475.
[19] L. Jing, F. Yang, L.M. Zhao, Perforation resistance of sandwich panels with layered gradient metallic foam cores, Compos. Struct. 171 (2017) 217–226.
[20] S.Q. Li, G.X. Lu, Z.H. Wang, L.M. Zhao, G.Y. Wu, Finite element simulation of metallic cylindrical sandwich shells with graded aluminum tubular cores subjected to internal blast loading, Int. J. Mech. Sci. 96–97 (2015) 1–12.
[21] I. Maskery, N.T. Aboulkhair, A.O. Aremu, C.J. Tuck, I.A. Ashcroft, R.D. Wildman, R.J.M. Hague, A mechanical property evaluation of graded density Al-Si10-Mg lattice structures manufactured by selective laser melting, Mater. Sci. Eng. A-Struct. 670 (2016) 264–274.
[22] L. Jing, K. Liu, X.Y. Su, X. Guo, Experimental and numerical study of square sandwich panels with layered-gradient foam cores to air-blast loading, Thin-Walled Struct. 161 (2021).
[23] H.Y. Zhou, Y.H. Wang, X.J. Wang, Z.Y. Zhao, G.W. Ma, Energy absorption of graded foam subjected to blast: a theoretical approach, Mater. Des. 84 (2015) 351–358.
[24] H. Lin, L. Lv, J.J. Zhang, Z.H. Wang, Energy-absorbing performance of graded Voronoi foams, J. Cell. Plast. 55 (6) (2019) 589–613.
[25] L.Q. Tang, X.P. Shi, L. Zhang, Z.J. Liu, Z.Y. Jiang, Y.P. Liu, Effects of statistics of cell's size and shape irregularity on mechanical properties of 2D and 3D Voronoi foams, Acta Mech. 225 (4-5) (2014) 1361–1372.
[26] H.X. Zhu, J.R. Hobdell, A.H. Windle, Effects of cell irregularity on the elastic properties of 2D Voronoi honeycombs, J. Mech. Phys. Solid. 49 (4) (2001) 857–870.
[27] Y.Z. Song, Z.H. Wang, L.M. Zhao, J. Luo, Dynamic crushing behavior of 3D closed-cell foams based on Voronoi random model, Mater. Des. 31 (9) (2010) 4281–4289.
[28] K. Li, X.L. Gao, G. Subhash, Effects of cell shape and strut cross-sectional area variations on the elastic properties of three-dimensional open-cell foams, J. Mech. Phys. Solid. 54 (4) (2006) 783–806.
[29] S.F. Liao, Z.J. Zheng, J.L. Yu, Dynamic crushing of 2D cellular structures: local strain field and shock wave velocity, Int. J. Impact Eng. 57 (2013) 7–16.
[30] X.P. Shi, S.Y. Liu, H.L. Nie, G.X. Lu, Y.L. Li, Study of cell irregularity effects on the compression of closed-cell foams, Int. J. Mech. Sci. 135 (2018) 215–225.
[31] Y.D. Wu, L.Q. Tang, Z.J. Liu, Y.P. Liu, Z.Y. Jiang, X.Y. Zhang, Numerical study of the shape irregularity gradient in metallic foams under different impact velocities, J. Mater. Eng. Perform. 26 (8) (2017) 3892–3900.
[32] Y. Hu, Q.Z. Fang, J. Qian, Effect of cell structure on the uniaxial compression properties of closed-cell foam materials, Mater. Today Commun. 26 (2021), 102104.
[33] A.H. Brothers, D.C. Dunand, Mechanical properties of a density-graded replicated aluminum foam, Mater. Sci. Eng. A-Struct. 489 (1-2) (2008) 439–443.
[34] A. Kemény, N. Movahedi, T. Fiedler, J.E. Maróti, I.N. Orbulov, The influence of infiltration casting technique on properties of metal syntactic foams and their foam-filled tube structures, Mater. Sci. Eng. A-Struct. 852 (2022), 143706.
[35] A.D. Akinwekomi, Microstructural characterisation and corrosion behaviour of microwave-sintered magnesium alloy AZ61/fly ash microspheres syntactic foams, Heliyon 5 (4) (2019), e01531.
[36] T. Fiedler, I.V. Belova, G.E. Murch, On the thermal properties of expanded perlite-Metallic syntactic foam, Int. J. Heat Mass Transfer 90 (2015) 1009–1014.
[37] N. Movahedi, T. Fiedler, A. Taşdemirci, G.E. Murch, I.V. Belova, M. Güden, Impact loading of functionally graded metal syntactic foams, Mater. Sci. Eng. A-Struct. 839 (2022), 142831.
[38] X.Z. An, Y.K. Gao, J.G. Fang, G.Y. Sun, Q. Li, Crashworthiness design for foam-filled thin-walled structures with functionally lateral graded thickness sheets, Thin-Walled Struct. 91 (2015) 63–71.
[39] H. Liu, Z.Q. Zhang, H. Liu, J.L. Yang, H. Lin, Theoretical investigation on impact resistance and energy absorption of foams with nonlinearly varying density, Compos. B Eng. 116 (2017) 76–88.
[40] X.Y. Zhang, L.Q. Tang, Z.J. Liu, Z.Y. Jiang, Y.P. Liu, Y.D. Wu, Yield properties of closed-cell aluminum foam under triaxial loadings by a 3D Voronoi model, Mech. Mater. 104 (2017) 73–84.
[41] A. Szlancsik, B. Katona, K. Bobor, K. Májlinger, I.N. Orbulov, Compressive behaviour of aluminium matrix syntactic foams reinforced by iron hollow spheres, Mater. Des. 83 (2015) 230–237.
[42] K. Májlinger, I.N. Orbulov, Characteristic compressive properties of hybrid metal matrix syntactic foams, Mater. Sci. Eng. A-Struct. 606 (2014) 248–256.

[43] Y. Duan, X.H. Zhao, Z.Y. Liu, N.D. Hou, H.F. Liu, B. Du, B. Hou, Y.L. Li, Dynamic response of additively manufactured graded foams, Compos. B Eng. 183 (2020), 107630.
[44] J.J. Zhang, Z.H. Wang, L.M. Zhao, Dynamic response of functionally graded cellular materials based on the Voronoi model, Compos. B Eng. 85 (2016) 176–187.
[45] C.H. Rycroft, G.S. Grest, J.W. Landry, M.Z. Bazant, Analysis of granular flow in a pebble-bed nuclear reactor, Phys. Rev. E 74 (2006), 021306.
[46] X.Y. Zhang, Y.D. Wu, L.Q. Tang, Z.J. Liu, Z.Y. Jiang, Y.P. Liu, H.F. Xi, Modeling and computing parameters of three-dimensional Voronoi models in nonlinear finite element simulation of closed-cell metallic foams, Mech. Adv. Mater. Struct. 25 (15-16) (2018) 1265–1275.
[47] Y.D. Wu, D. Qiao, L.Q. Tang, Z.J. Liu, Y.P. Liu, Z.Y. Jiang, L.C. Zhou, Global topology of yield surfaces of metallic foams in principal-stress space and principal-strain space studied by experiments and numerical simulations, Int. J. Mech. Sci. 134 (2017) 562–575.
[48] Y.D. Wu, D. Qiao, L.Q. Tang, H.F. Xi, Y.P. Liu, Z.Y. Jiang, Z.J. Liu, L.C. Zhou, Global topology of failure surfaces of metallic foams in principal-stress space and principal-strain space studied by numerical simulations, Int. J. Mech. Sci. 151 (2019) 551–562.
[49] J. Miltz, G. Gruenbaum, Evaluation of cushioning properties of plastic foams from compressive measurements, Polym. Eng. Sci. 21 (15) (1981) 1010–1014.
[50] Z.J. Zheng, C.F. Wang, J.L. Yu, S.R. Reid, J.J. Harrigan, Dynamic stress–strain states for metal foams using a 3D cellular model, J. Mech. Phys. Solid. 72 (2014) 93–114.